Supplementary Information

Persistent organic carbon storage in river floodplains over millennia

Yutian Ke[1*], A. Joshua West[2], Emily C. Geyman[1], Katie Ann Huy[1,3], Hannah Dion-Kirschner[1], M. Isabel Smith[1], Joshua S. Anadu[1], John S. Magyar[1], Michael P. Lamb[1], Woodward W. Fischer[1]

1. Division of Geological and Planetary Sciences, California Institute of Technology, Pasadena, CA 91125 USA
2. Department of Earth Sciences, University of Southern California, Los Angeles, CA 90089, USA
3. Present address: Department of Earth System Science, Stanford University, Stanford, CA 94305, USA

[*]To whom correspondence should be addressed: yutianke@caltech.edu

Contents of this file

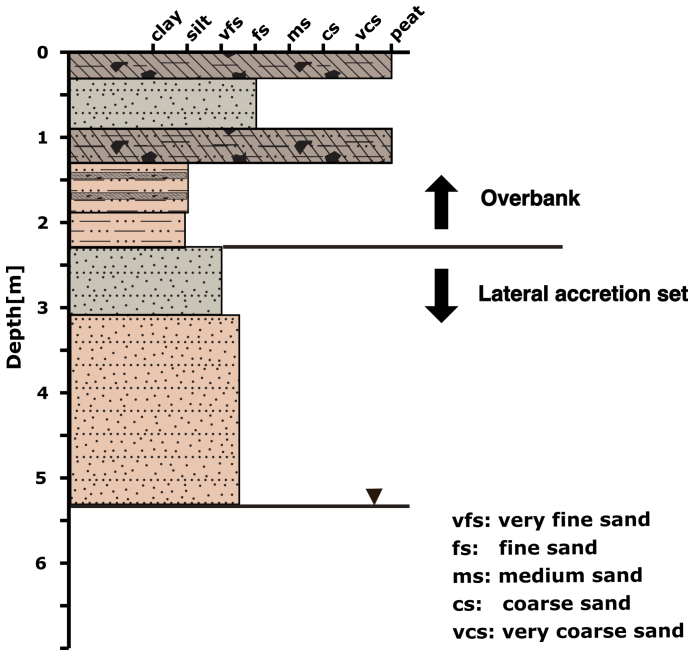

Figure S1. Stratigraphic section illustrating typical riverbank stratigraphy exposed along the Koyukuk River near Huslia, Alaska. Overbank deposition typically consists of fine-grained sediments and organic-rich materials (e.g. litter and peat), accumulated during flood events. In contrast, lateral accretion sequences (LAS) form through river migration, depositing sandier sediments that at or below the water table. Here, thickness refers to the vertical interval measured from the basal stratigraphic boundary of the LAS to the elevation of the river thalweg.

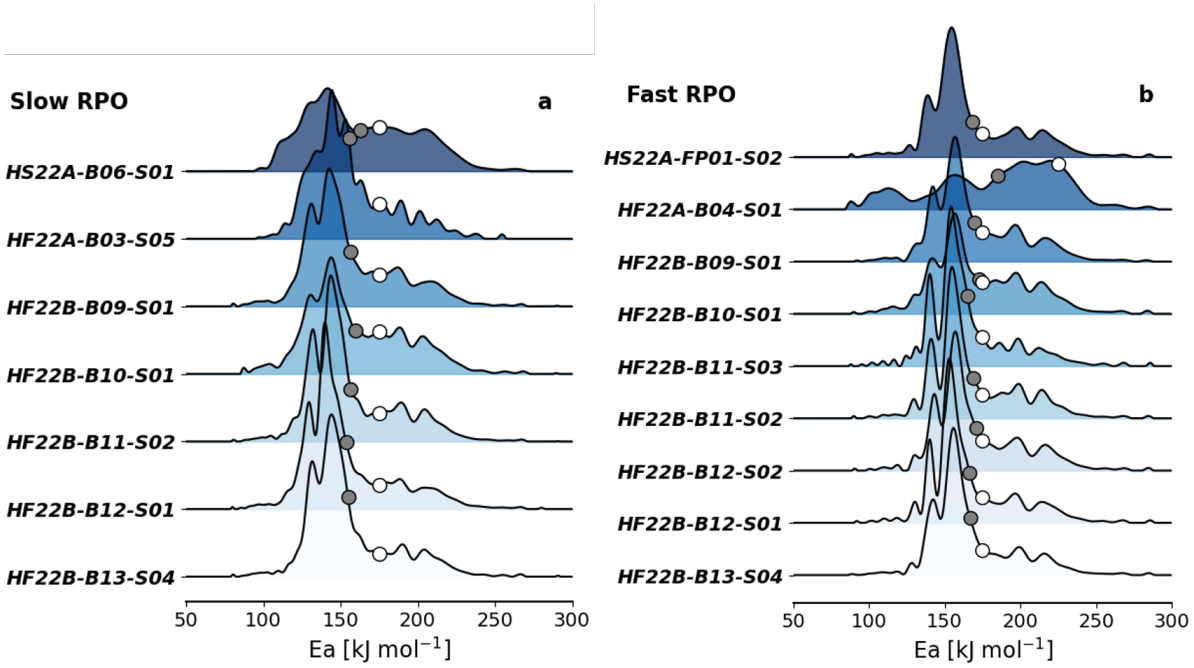

Figure S2. *p*(E) distribution for organic carbon (OC) in LAS deposits using (a) Slow-RPO and (b) Fast-RPO methods. The similarity in distribution modes across profiles indicates broadly comparable OC composition among different LAS deposits. White circles represent mean Ea values, while grey circles denote median Ea values.

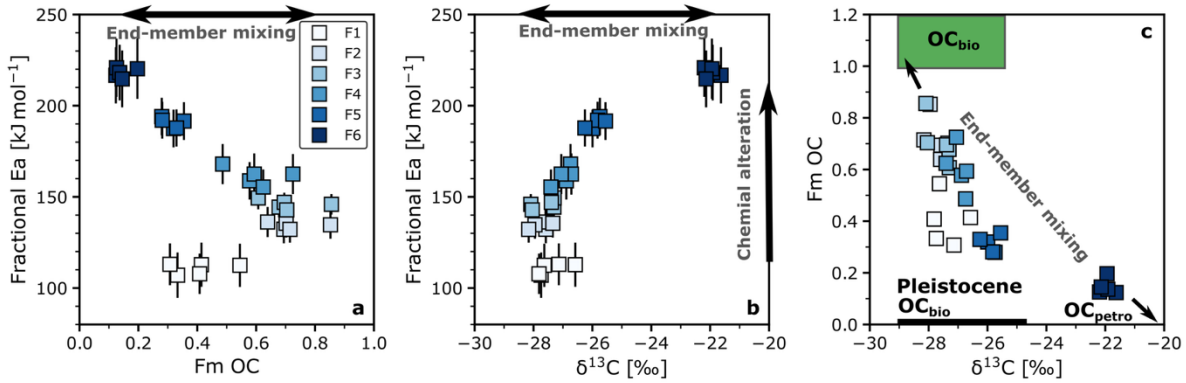

Figure S3. Thermal and isotopic parameters of gas fraction obtained from Slow-RPO. Panels (a) and (b) show systematic inter- and intra-sample variation of fractional energy with Fm and $\delta^{13}C$. Panel (c) shows the mixing space of $\delta^{13}C$ and Fm with the two obvious endmembers: OC_{bio} and OC_{petro}. The black bar indicates the range of Yedoma organic carbon (Fm: 0–0.02; $\delta^{13}C$: −29.0‰ to −24.7‰)[72], representing Pleistocene OC_{bio}. The green bar represents Arctic terrestrial biomass (Fm: 1.00–1.20; $\delta^{13}C$: −29.0‰ to −26.4‰)[73], shown as an example of the modern OC_{bio} end-member. Colour denotes different gas fractions, 6 gas fractions were collected for each sample OC using Slow-RPO. F1 is characterised by low activation energy and low Fm and depleted $\delta^{13}C$. Larger fractional μ_E shows the relatively more refractory nature of the OC compound mixing. The error bar represents ± 1 fractional σ_E. Arrows indicate the endmember mixing by the change of carbon isotopic values, and the chemical alteration by the change of activation energy of different gas fractions.

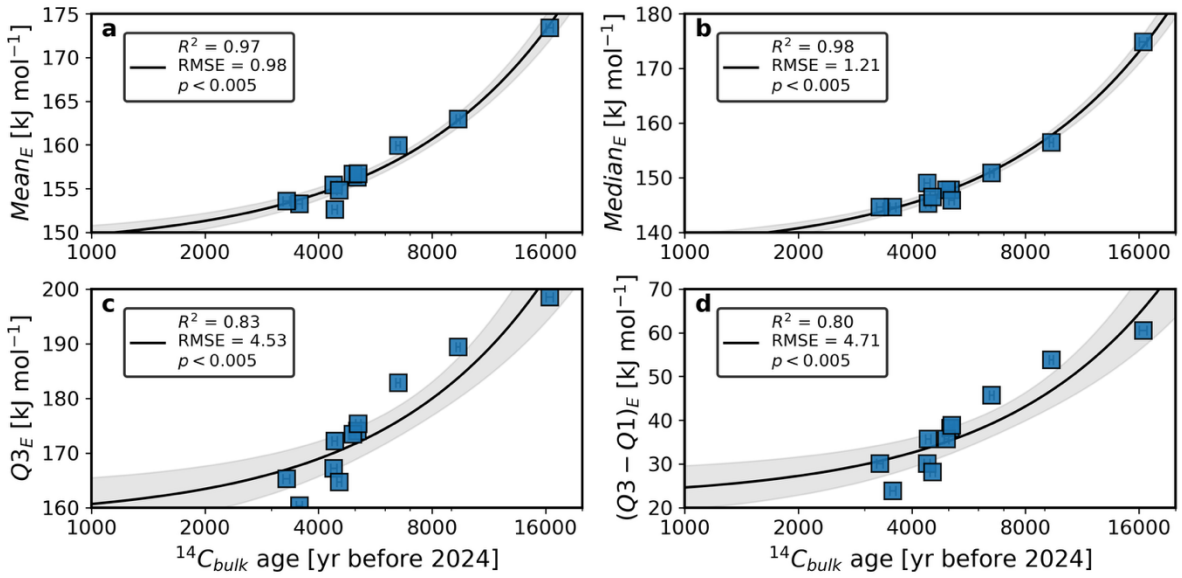

Figure S4. Correlation of activation energy (E) parameters with bulk radiocarbon age of organic carbon ($^{14}C_{bulk}$ age): (a) mean E (μ_E), (b) median E, (c) 75th percentile (Q3) of E, and (d) interquartile range (Q3–Q1) of E, Q1 is the 25th percentile of Ea. All Ea parameters were determined from spectra acquired via Slow-RPO mode. Error bars denote 1σ, and the black line represents a least squares linear regression with a high R^2, signifying that Ea increases as the $^{14}C_{bulk}$ age increases. All regressions have a p-value < 0.005, confirming their statistical significance. The low root squared standard error (RMSE) across parameters suggests a strong predictive accuracy for Ea values.

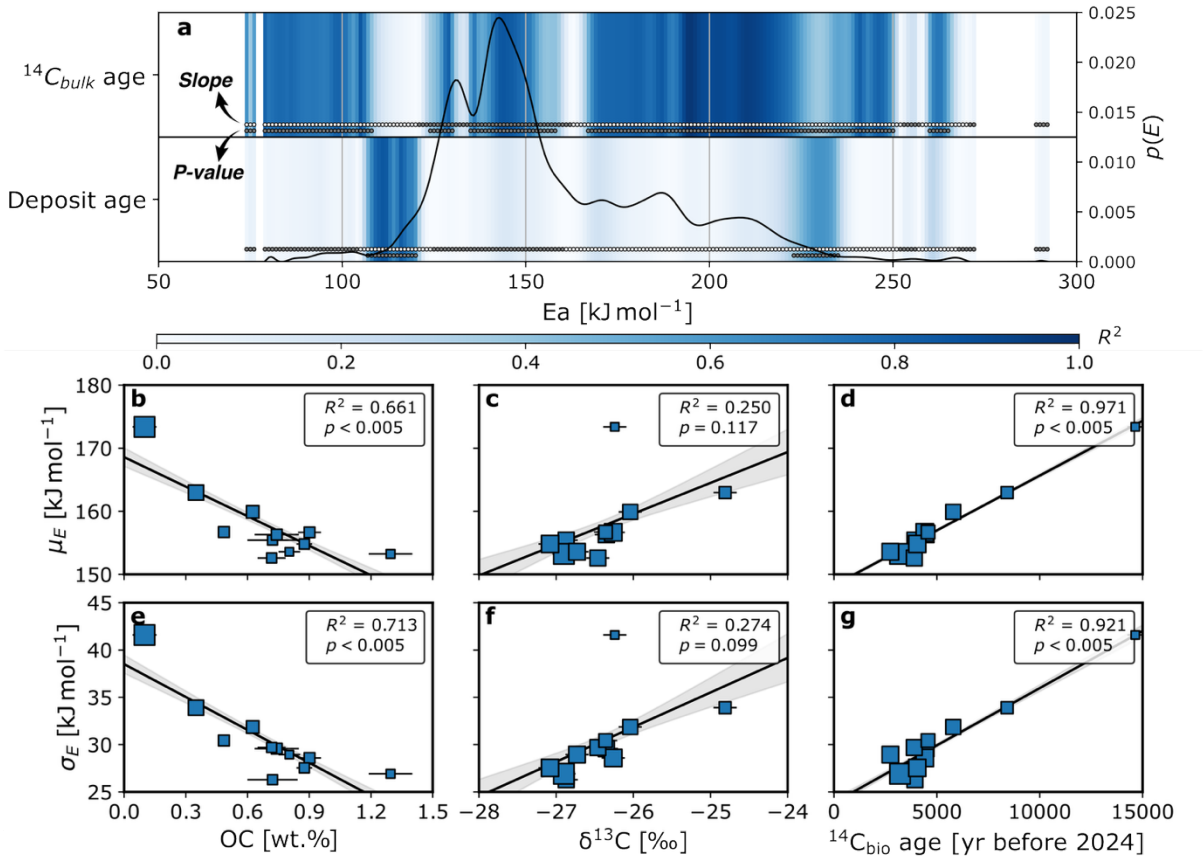

Figure S5. Correlation of p(E) variation for Ea (1 kJ mol^{-1} interval) with different timescales: radiocarbon age of bulk OC ($^{14}C_{bulk}$) age and deposit age (a). Complete dataset including Slow-RPO and shifted Fast-RPO; b. Fast-RPO samples; c. a subset of samples by removing HS22A-B06-S01 (outlier deposit age). The color bar indicates the adjusted R^2 of the linear regression at each Ea value. For each age category, two dotted lines are plotted: the top line (solid, black and white) shows the slope of the regression (black indicating positive, white indicating negative correlations), and the bottom line (intermittent black) shows the corresponding p-values from a t-test. Black segments on the p-value line denote statistically significant correlations ($p < 0.005$); no color indicates non-significance. The black curve is an example Ea distribution for OC from one sample. Panels (b), (d) and (f) show systematic decrease of OC (wt.%) and increase of $\delta^{13}C$ and biospheric OC ($^{14}C_{bio}$) ages (relative to 2024) accompanied with the increasing mean activation energy (μ_E); (c), (e) and (g) show decrease of OC (wt.%) and increase of $\delta^{13}C$ and $^{14}C_{bio}$ ages accompany with the accompanied with the standard deviation of energy distribution (σ_E) decreasing. Scatter size in (b) and (c) represents scale variation of Fm_{bio} and is OC wt.% in (d), (e), (f), and (g). The error bar represents ± 1σ (standard deviation); the black line represents the least-squares linear regression, and the shaded area in grey is the 90% confidence interval of the regression.

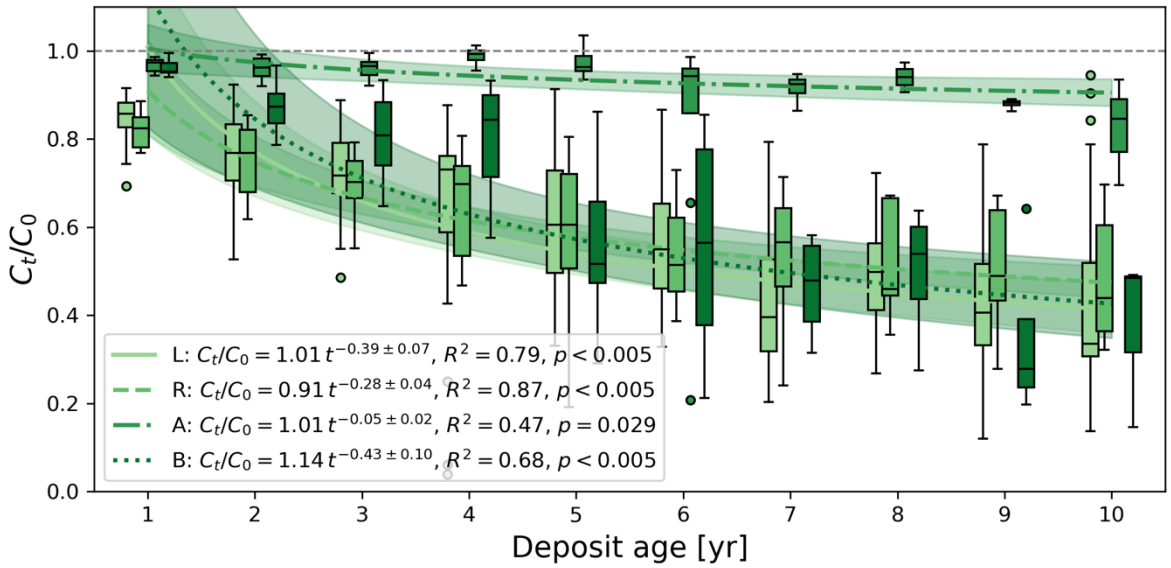

Figure S6. Carbon degradation in the Long-Term Intersite Decomposition Experiment (LIDET) at Bonanza Creek over a decade. Plant components include L (leaves; see also Figure 4), R (roots), A (aboveground wood), and B (belowground wood). All four components exhibited measurable degradation over the 10-year experimental period[36]. A log-linear regression was fitted using the median values of each group, with the shaded area indicating the 90% confidence interval.

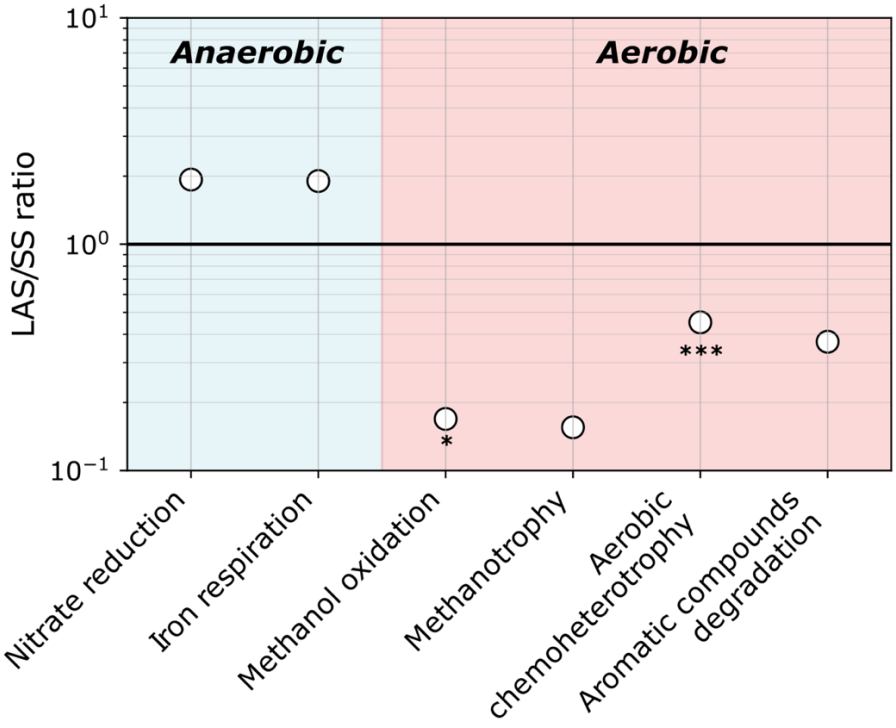

Figure S7. Relative abundances of microbial function groups between lateral accretion sequences (LAS) sediment and suspended sediment (SS) highlighted the prevalence of anaerobic metabolic modes in the floodplain deposits compared to suspended sediment in transit. To illustrate which microbial metabolic functions are enriched in LAS deposits, we compared predictions from microbial community sequence data extracted from LAS samples (n = 43) to suspended sediment samples collected in river depth profiles at the same time (n = 29), expressed as the LAS/SS ratio. Asterisk ratings mark the p values: $p < 0.05^{*}$, and $p < 0.005^{***}$. Six key functions were categorized: nitrate reduction, iron respiration, methanol oxidation, methanotrophy, aerobic chemoheterotrophy, and aromatic compounds degradation. See Methods for details.

Text S1

Supplement methods

River migration rate calculation

To quantify rates of river migration, we adopted the methodology outlined by Sylvester et al. (2019)[1]. Briefly, optical satellite images (Landsat images from 1986 and 2015) were converted into binary masks distinguishing the river from its surrounding floodplain (see Fig. S8). Differencing the two binary masks produces estimates of the accreted area and eroded area, facilitating the quantification of planform river change in complex, multithreaded rivers (Fig. S8[2]). Given that the Koyukuk River is single-threaded, we use morphological erosion to thin each binary mask (from 1986 and 2015) into a skeletonized single-pixel-wide centerline by employing the 'bwskel' function in MATLAB[3]. Subsequently, we used the dynamic time warping (DTW) technique[4] to quantify the migration distance between the centerlines from the two time points (Fig. S9)[1,5]. This analysis was performed in MATLAB using the 'dtw' function. The local river migration distance was determined based on the length of the dynamic time warping vectors that linked the centerline from 1978 with that from 2015 (as

shown in Fig. S9). For the period spanning 1986 to 2015, the average migration rate of the river in the study region was 2.07 m yr^{-1}. Through lateral migration, the river constantly erodes on its outer bank a portion of the river floodplain that tends to be old (and, in Arctic landscapes, perennially frozen–i.e., permafrost) and deposits on the inner bank a portion of new floodplain material that is initially unfrozen. Such dynamics can lead to the release of OC that was previously sequestered in the permafrost deposits. The methodological framework is outlined in Geyman et al. (2024)[6], with supporting data archived in the Arctic Data Center[7].

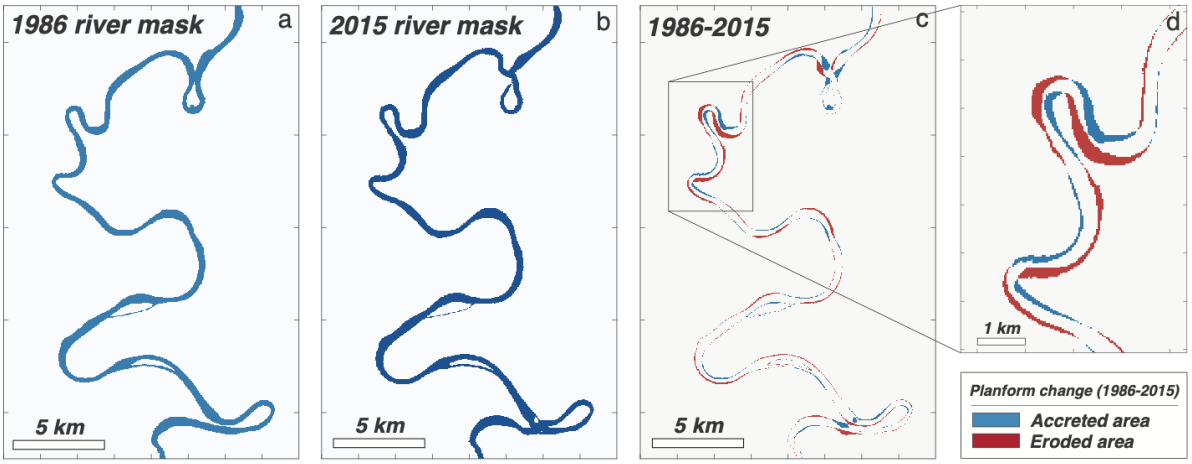

Figure S8. Workflow for detecting river migration from timelapse satellite imagery. (a-b) Landsat satellite images (30 m spatial resolution) from 1986 and 2015 are transformed to binary masks of river vs. floodplain using simple spectral thresholding. (c-d) Overlaying the co-registered binary river masks from 1986 and 2015 reveals the eroded and accreted areas.

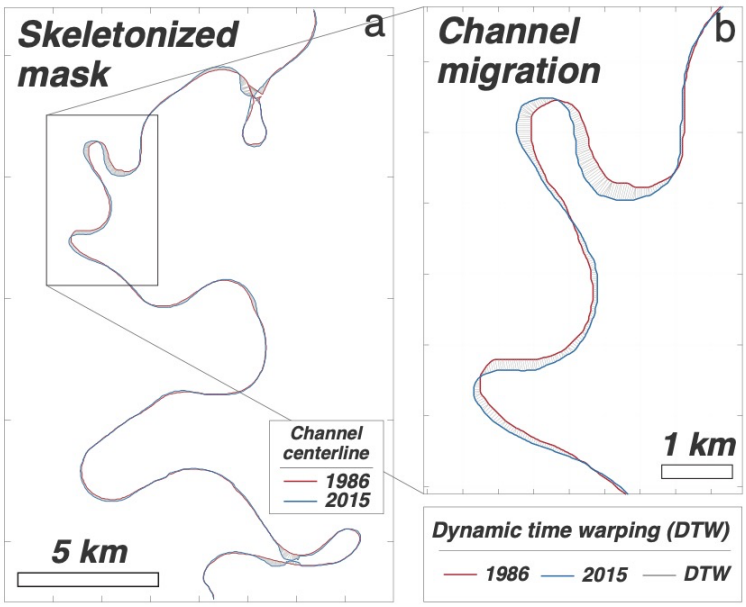

Figure S9. An illustration of measuring channel migration rates using dynamic time warping (DTW) applied to channel centerlines[1,5]. (a) First, we skeletonize the river masks (thin the binary masks to a one-pixel-wide skeleton along the channel centerline. (b) We sort the channel centerline positions from times t1 and t2 (1986 and 2015) by river longitudinal distance (upstream to downstream), and then use dynamic time warping (DTW) to measure the local channel migration vectors. The average river migration rate in the region shown for the period 1986-2015 is 2.07 m yr^{-1}.

Floodplain deposit/terrain age model

In spring (June) and fall (September) of 2022, we surveyed 43 stratigraphic sections along exposed riverbanks near Huslia to investigate near-surface floodplain deposits (Fig. S10, Supplementary Data 1). A total of 40 discrete organic fragments were collected from lateral accretion (LAS) deposits for radiocarbon dating, which provided age constraints used to construct a floodplain terrain age model (Fig. S10) and to calibrate the backtracking reconstruction of channel migration (Fig. S11). The resulting terrain age map includes ten distinct age categories, ranging from the present to approximately 20,000 years before present, based on radiocarbon-dated materials. We collected 187 bank sediment samples from the stratigraphic sections: 62 from LAS deposits, 104 from overbank deposits, and 21 from old channel fills. To constrain the sedimentological characteristics of LAS deposits, grain size distributions were analyzed for 49 of the 61 LAS samples. One sample was excluded due to a high concentration of visually observed discrete organic debris; the remaining samples were used to quantify the mud fraction and were used to build Figure 3a. Each LAS sample was assigned a depositional age to enable subsequent OC degradation calculations. Age assignments were made using three approaches: direct radiocarbon dating (12 samples), backtracking-based channel migration modeling (24 samples), and floodplain terrain age interpolation (12 samples). The most reliable age estimate for each section was selected for statistical analysis and degradation model calculations.

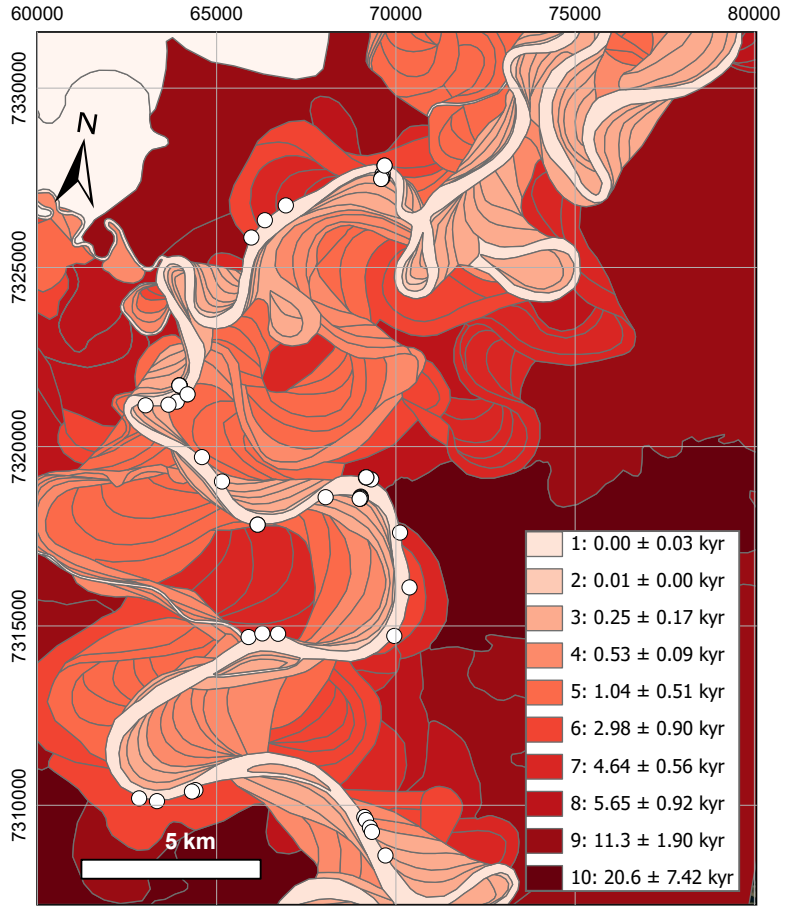

Figure S10. Floodplain deposit age model adapted from Geyman et al. (2025)[8]. Circles indicate locations where bank sediments were sampled. Deposits from abandoned channel fills were excluded due to the absence of lateral accretion sets. Floodplain age is represented by color, with darker tones indicating older surfaces. Each color corresponds to a distinct age class, reported in the legend as the mean ± 1σ.

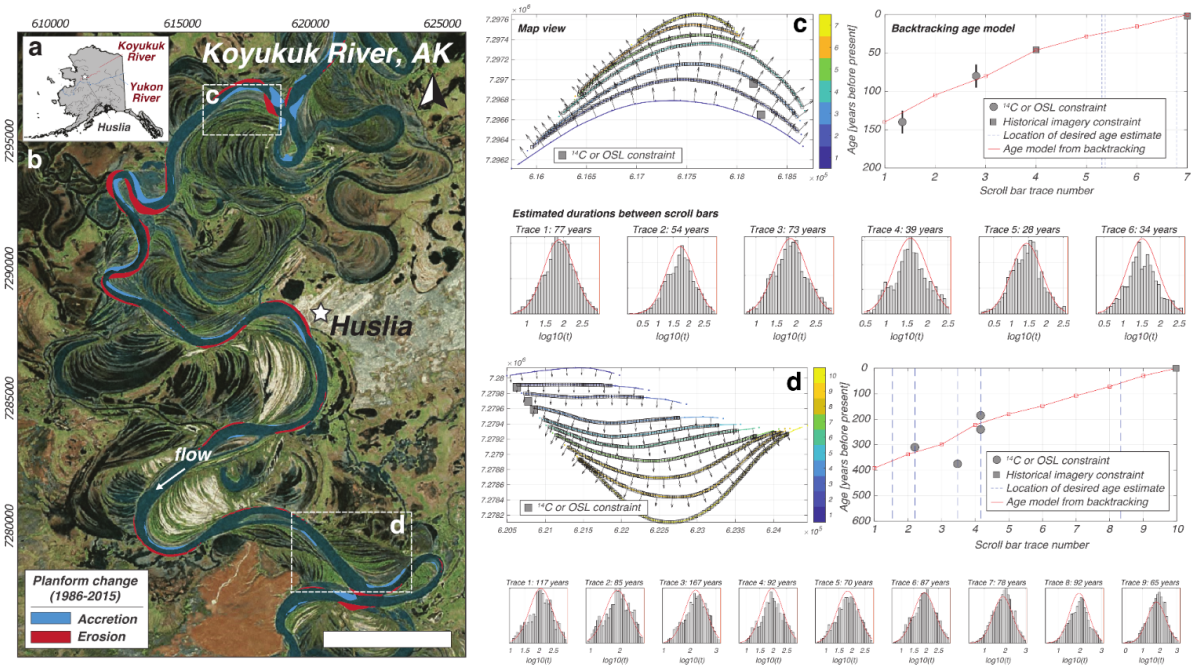

Figure S11. Examples of the channel backtracking approach employed here to estimate the ages of floodplain deposits. Panels (a-b) show the study area, with two highlighted squares indicating the locations of the detailed examples shown in (c-d). The scroll bar geometry in panels (c-d) delineates successive riverbank positions, representing modern and historical river migration. Numbers denote the identified scroll bars, increasing from older to younger surfaces. This numbering corresponds to the relative age of bank deposits and is consistent with the colour gradient shown in the accompanying colour bar. Grey squares mark locations where we have ^{14}C or OSL age constraints. The backtracking age model shows good consistency with the geochronological controls. Histograms show the estimated time interval between scroll bars, representing the duration of the corresponding lateral accretion events. The base map in (b) is sourced from Sentinel-2 satellite imagery (European Space Agency), and the coordinates are in UTM zone 4N.

Permafrost probing

In the field, we determined the frozen or thawed state of the deposits in early fall, mapping at a time when the active layer is at its deepest. To confirm the presence of permafrost, we physically probed the ground using a 1 m- or 2 m-long metal permafrost probe, which allowed us to determine both the presence and the depth of the underlying layer, known as the permafrost surface. We inferred the presence of permafrost when the probe encountered a hard surface, marking the presence of persistent pore ice. We observed permafrost at detectable depths in the scroll bars of relatively old deposit age (in the middle of HF22B-B11 and HF22B-B12); however, in the more recently built scroll bars, permafrost was not detected from either vertically probing from the top or laterally from the exposed bank face. Our field observations of permafrost presence/absence from summer 2018 and fall 2022 were published on the ESS-DIVE repository[9].

Normalized cross-correlation method

The same sediment organic carbon (OC) sample yielded differing $p(E)$ distributions when analyzed using Fast-RPO and Slow-RPO methods (Supplementary Data 3). To quantify the systematic phase lag between the two,

we applied normalized cross-correlation analysis (Fig. S12a). The cross-correlation $R_{S-F}(\tau)$ of $p_S[E]$ and $p_F[E]$at lag τ was calculated by ensuring the correlation coefficient was scaled within the range [-1, 1], regardless of the magnitude of the individual values in each p(E) distribution, following:

$$R_{S-F}(\tau) = \frac{\sum_{E_i}(p_S[E_i]-\underline{p_S})(p_F[E_i+\tau]-\underline{p_F})}{\sqrt{\sum_{E_i}(p_S[E_i]-\underline{p_S})^2(p_F[E_i+\tau]-\underline{p_F})^2}} \quad (1)$$

where E_i is the i-th Ea value, $\underline{p_S}$ and $\underline{p_F}$ are the means of $p_S[E]$ and $p_F[E]$respectively. The phase lag is the amount of shift needed for the two p(E) distributions to align at this point of maximum correlation. The index-based phase lag ∇L_i is calculated after finding the index of the maximised correlation, where two p(E) distributions are most similar, as:

$$\nabla L_i = argmax\tau R_{S-F}(\tau) - (N_F - 1) \quad (2)$$

where N_F is the length of Ea from the Fast-RPO. Then ∇L_i was converted to E-based phase lag ∇L_E, which is scaled by the spacing of the Ea values:

$$\nabla L_E = \frac{\nabla L_i}{N_F}(max(E) - min(E)) \quad (3)$$

This method allowed us to calibrate the p(E) distribution from Fast-RPO to match that of the Slow-RPO, ensuring consistency across analytical protocols (Fig. S12b). The calculated phase lag was used to adjust the cutoff Ea for partitioning OC_{bio} and OC_{petro} (Fig. S13). Applying this correction to the p(E) distributions from Fast-RPO yielded strong agreement with those from Slow-RPO, further validating the use of normalized cross-correlation for alignment (Fig. S14).

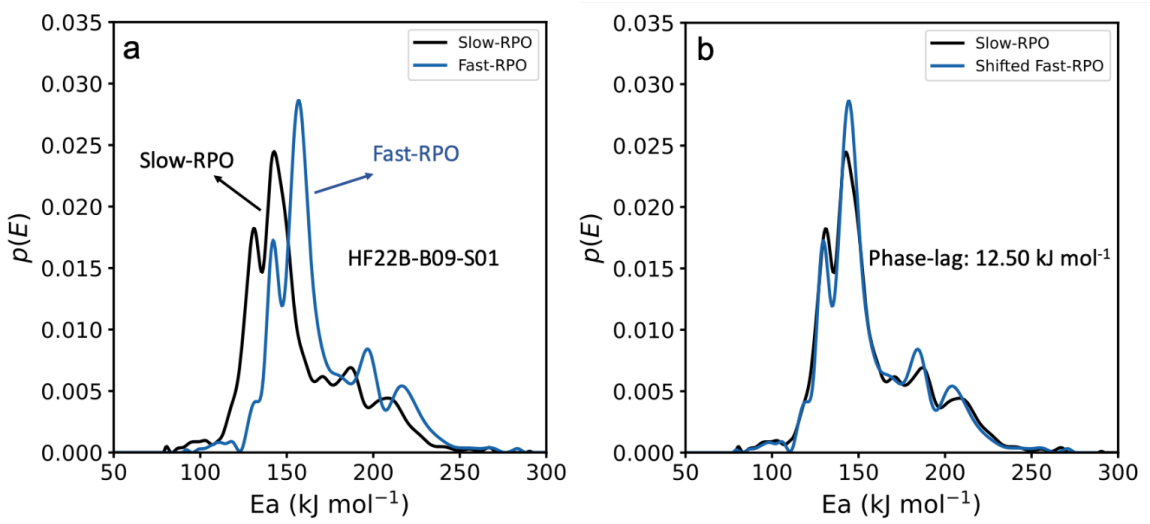

Figure S12. Analysis of normalised cross-correlation of p(E) distribution between Fast-RPO and Slow-RPO modes. Phase lags were identified for each sample, with HF22B-B09-S01 showcased as a representative example. (a) illustrates significant differences in the pre-calibrated p(E) distribution between the two modes. The identified E-based phase lag for Fast-RPO is -12.5 kJ mol^{-1} post-calibration, (b) demonstrates a strong alignment of the p(E) distribution between two modes post-calibration. The original and shifted Fast-RPO are denoted in blue lines, and the Slow-RPO is represented by the black line.

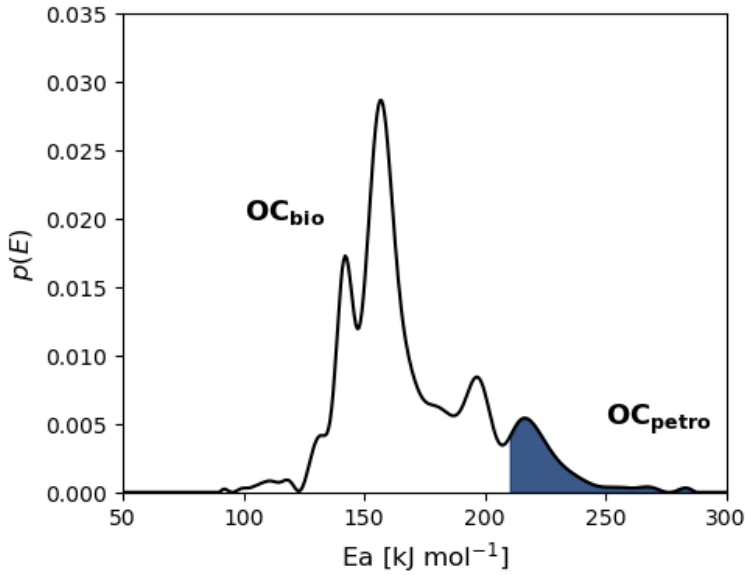

Figure S13. Representative *p*(E) distribution from a Slow-RPO analysis, illustrating the use of a cutoff activation energy value to determine OC_{bio} (in white) and OC_{petro} (in blue).

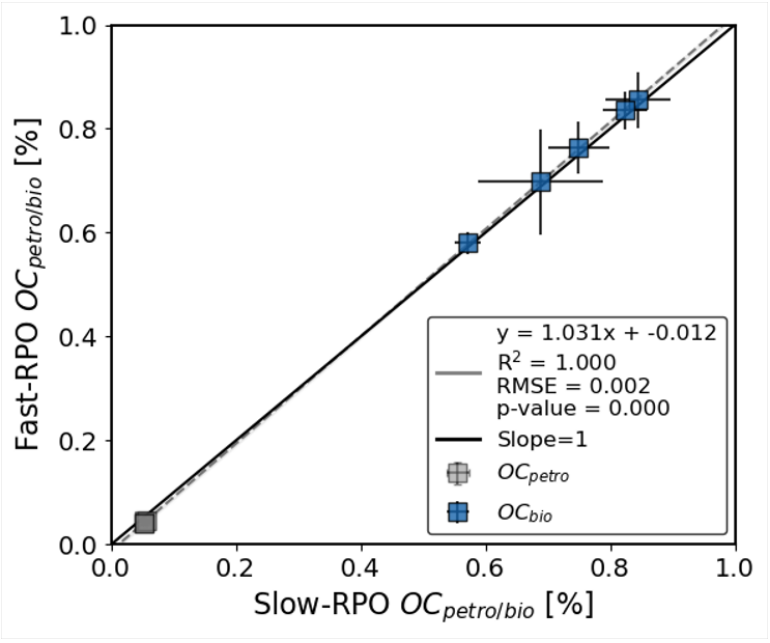

Figure S14. Validation of normalized cross-correlation outcomes. Five sediment samples were analyzed using both Fast-RPO and Slow-RPO. For each pair, the phase lag in the *p*(E) distribution was calculated to get the corresponding calibration. After calibration, the estimated OC_{bio} and OC_{petro} content from Fast-RPO align with those derived from the Slow-RPO. The error bar represents 1σ.

Gas Chromatography-Mass Spectrometry (GC-MS) analysis

To assess the provenance of solvent-extractable organics in sediments collected from scroll bar complexes, lipids were extracted from freeze-dried aliquots from two samples (HF22B-B09-S01 and HF22B-B12-S01) utilising a CEM MARS® 5 microwave-accelerated reaction system. Samples in a solution of 9:1 v/v dichloromethane:methanol mixture were heated to 100 °C over a 10-minute duration, maintained at this temperature for 20 minutes, and then allowed to cool gradually. The resultant total lipid extracts were filtered to

remove particulate matter, followed by hydrolysis via base saponification. Hydrolyzed total lipid extracts were deposited on solid phase extraction columns (Sepra NH_2, Phenomenex) and hydrocarbons were eluted in hexanes. Hydrocarbons were targeted as the compound class of interest owing to their distinctive distribution profiles that are commonly used as biomarkers for terrestrial plant matter, and other hydrocarbon compounds may indicate the presence of common petrochemical contaminants. Hydrocarbon compounds were characterised and quantified using a Thermo Scientific Trace GC Ultra gas chromatograph with a Zebron ZB-5 30 m × 0.25 mm ID × 0.25 μm film thickness column, coupled to a Thermo ISQ LT single quadrupole mass spectrometer. The GC oven program proceeded as follows: hold at 70 °C for 1 minute, ramp at 20 °C per minute for 3 minutes, then ramp at 5 °C per minute for 38 minutes, and a final hold at 320 °C for 20 minutes. Compounds were identified by comparing mass spectral fragments with internal and NIST libraries, as well as by retention time. Peak detection was automated in Xcalibur using the Genesis algorithm to integrate all peaks with intensity ≥0.5% of the maximum intensity peak within that chromatogram, and then manually curated to discard any peaks that were not fully resolved from the baseline.

Microbial genomics

LAS and suspended sediment samples were paired with a sample subset for microbial community analysis via 16S rRNA amplicon sequencing. Sediment samples were frozen the day of collection and maintained frozen until analysis; some samples were preserved in Qiagen PowerSoil Pro bead tubes with 800 μL of Qiagen LifeGuard Soil Preservation Solution. This preservative stopped microbial activity and helped maintain the stability of nucleic acids in the samples until their analysis in the laboratory at Caltech. DNA was extracted from sediment samples using the Qiagen PowerSoil Pro Kit, following the manufacturer's instructions. As necessary, an adjustment was made during the sample loading and lysis step to accommodate the presence of the added LifeGuard preservative. Sediment samples in bead tubes with the preservative were centrifuged, and the preservative was decanted from the samples. Lysis buffer was then added to the pelleted samples in the bead tubes, and the procedure continued following the manufacturer's instructions. For suspended sediments collected on PES filters, a representative portion of the filter was cut out and placed directly in bead tubes for extraction. For suspended sediments collected in Sterivex filter units, 1 mL of lysis buffer was added directly to the Sterivex unit through the inlet, ends capped, and vortexed at minimum speed for 10 minutes. After vortexing, the buffer was removed from the inlet using a syringe and added to the bead tubes. The procedure then continued following the manufacturer's instructions.

The V4-to-V5 region of the 16S ribosomal subunit was Polymerase Chain Reaction (PCR)-amplified using 515f (GTGYCAGCMGCCGCGGTAA) and 926r (CCGYCAATTYMTTTRAGTTT) primers, which had Illumina adaptors appended to their 5' ends. PCR reactions were prepared with 12.5 μL Q5 Hot Start High-fidelity 2X Master Mix (New England Biolabs), 9.0 μL nuclease-free water, 1.25 μL forward primer (10 μM), 1.25 μL (10 μM) reverse primer, and 1 μL DNA extract (1-10 ng/μL), for a total volume of 25 μL. PCR conditions are as follows: 2 min at 98 °C, 30 cycles of 10 s at 98 °C, 20 s at 54 °C, 20 s at 72 °C, followed by 2 min at 72 °C and hold at 4 °C. The success of the amplification reaction was confirmed through gel electrophoresis. Subsequently, 20 μL of each product was sent to Laragen for barcoding via PCR with Illumina Nextera XT primers, purification, and pooling in equal proportions. Finally, the pooled library was sequenced through 2 x 250-bp paired-end Illumina Miseq.

16S rRNA sequences were extracted from fastq files using CutAdapt (v.127), and reads were trimmed to remove adaptors and filtered to 240 bp for forward and 200 bp for reverse reads, with a minimum of 150 bp. Using QIIME with DADA2[10] and a custom *R* script following developers' recommendations[11] reads were merged with a minimum of 12 bp overlap, chimeric sequences were removed, and Amplicon Sequence Variants (ASVs) were inferred. Finally, taxonomy was assigned to 16S rRNA sequences through ASV alignment to the SILVA Train set (v.138.1). Singletons, unassigned, and eukaryotic ASVs were excluded, and taxa relative abundances were computed for each sample. Using the microeco 0.19.0 tutorial, the functional potential of taxa within each sample was estimated at the family level based on known functions of related members in the FAPROTAX database.

Text S2

Supplement Discussion

Organic compound analysis

Hydrocarbon extracts for the two analysed LAS sediments (Fig. S15) were predominantly composed of a homologous series of n-alkanes C_{20}-C_{33}, accounting for 87% and 95% of all identified compounds as assessed by peak area. Odd-numbered carbon n-alkanes, especially n-C_{27} alkane (33% and 43% of total hydrocarbons, respectively), were most abundant. This homologous series exhibiting a strong odd-over-even preference with a maximum at n-C_{27}, is a hallmark of terrestrial plant leaf waxes[12], including in high-latitude environments[13,14]. Additionally, a further 9% and 5% of each hydrocarbon extract were composed of terpenoids, including norabietane and pentacyclic triterpenoids, compounds nearly exclusively found in higher plants[15]. The remainder of the peaks identified in each sample (0-4% of total peak area) were attributable to common contaminants introduced during GC-MS analysis, e.g., siloxanes. No hydrocarbon compounds associated with petrochemicals, including cycloalkanes, hopanes, or aromatic compounds[16], were detected in either sample.

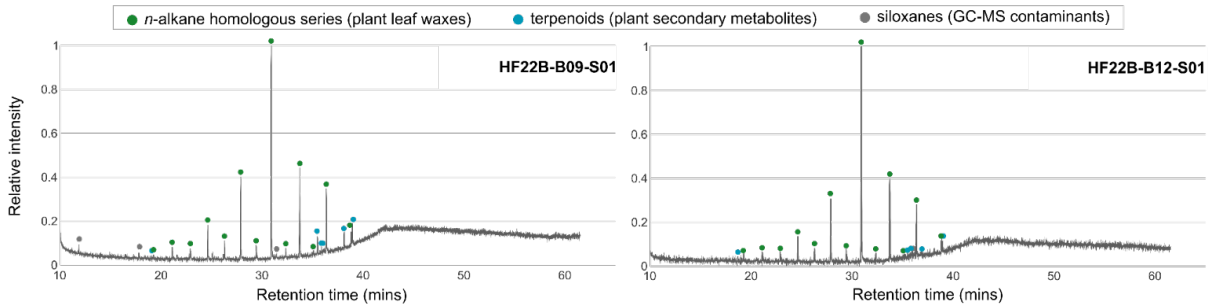

Figure S15. GC-MS analysis of lipids in scroll bar sediments, using samples HF22B-B12-S01 and HF22B-B09-S01 to represent young and old organic matter across the southern LAS deposit age spectrum (Figure 1d, f). The lipid biomarker compositions are highly similar between samples, despite differences in their age. Predominantly composed of *n*-alkanes C_{20}-C_{33} (87% and 95% by peak area), the hydrocarbon extracts also include 9% and 5% terpenoids, such as norabietane and a range of pentacyclic triterpenoids, respectively. This composition strongly suggests that plant-derived organic matter dominates in LAS deposits, with no evidence of hydrocarbon compounds associated with petrochemicals, including cycloalkanes, hopanes, or aromatic compounds.

Anaerobic environments common in LAS deposits

We characterized the microbial community composition using 16S rRNA amplicon sequencing and categorized taxa into six major functional groups: nitrate reduction, iron respiration, methanol oxidation, methanotrophy, aerobic chemoheterotrophy, and aromatic compounds degradation. To assess functional differences between depositional environments, we calculated the relative abundance ratio of each group between LAS and SS, expressed as the LAS/SS ratio. This comparison highlights the distinction between microbes associated with deeply buried, floodplain deposits (LAS) and those actively transported within the river system (SS). LAS samples were relatively enriched in anaerobic communities, including those capable of nitrate reduction under anoxic conditions and iron reduction using Fe(III) as a terminal electron acceptor in the absence of oxygen (Fig. S7, Supplementary Data 6). In contrast, SS contained a higher proportion of aerobic taxa that rely on dioxygen to oxidize organic substrates. These include pathways requiring O_2 for aromatic compound degradation, methanol oxidation to formaldehyde, and aerobic methanotrophy in which CH_4 is oxidized using O_2 as the electron acceptor.

Possible explanations for "F1"

In our observations, a minor proportion of OC (less than 3%) displayed high radiocarbon ages (4,878 - 9,480 ^{14}C yrs) and depleted ^{13}C composition (-27.81‰ - -26.51‰) coupled with low energy bonds inferred from Slow-RPO (107 - 110 kJ mol^{-1}) (Fig. S2, Supplementary Data 5) among 6 gas fractions (Fig. S16). This combination of moderate age, terrestrial $\delta^{13}C$ signature, and low average bond strength is atypical and falls within a range where OC becomes more reactive during extended storage in Arctic floodplain LASs. We refer to this distinct component as "F1," which has not been previously documented in sediments analyzed for RPO from terrestrial, aquatic, or fjord systems[17,18]. Gas chromatography-mass spectrometry analysis indicated no hydrocarbon contamination (e.g., aromatic compounds in crude oil or other petrochemical products), with spectra exclusively dominated by compounds associated with higher plant biomarkers (Fig. S15). A constant contamination (*ca*. 3.7 μg) with an Fm value of 0.555±0.042[19] from the RPO setup could not account for the lower Fm values in F1. The presence of this F1 component was puzzling, as labile OC might be expected to degrade readily during extended storage or transit in terrestrial environments[20,21]. We interpreted F1 as a mixture of (1) partially microbially reworked refractory OC, in which degradation processes reduced bond strength and induced slight $\delta^{13}C$ fractionation[22–25], (2) potentially a minor contribution from younger, more labile OC fractions, though radiocarbon evidence suggests this is not the dominant component, (3) Pleistocene-aged OC_{bio} remobilized from permafrost or ancient soils found across the Yukon Flats. This interpretation aligns with findings from permafrost and cryosol studies showing that Pleistocene OC_{bio} can be preserved for more than 30,000 years with $\delta^{13}C$ values in the range of –29.0‰ to –24.7‰[26]. Moreover, aged OC_{bio} has been shown to re-enter active biogeochemical cycling and exhibit altered reactivity in riverine and floodplain environments[17,27]. Compared to F1, the F2 (–28.16‰ to –27.35‰) and F3 (–27.30‰ to –28.09‰) fractions are more ^{13}C-depleted, while F4 (–27.41‰ to –26.71‰), F5 (–26.25‰ to –25.55‰), and F6 (–22.20‰ to –21.63‰) show progressively enriched values (Supplementary Data 5). The $\delta^{13}C$ range in F1 may therefore reflect both microbial processing and the isotopic imprint of mixed source contributions[28].

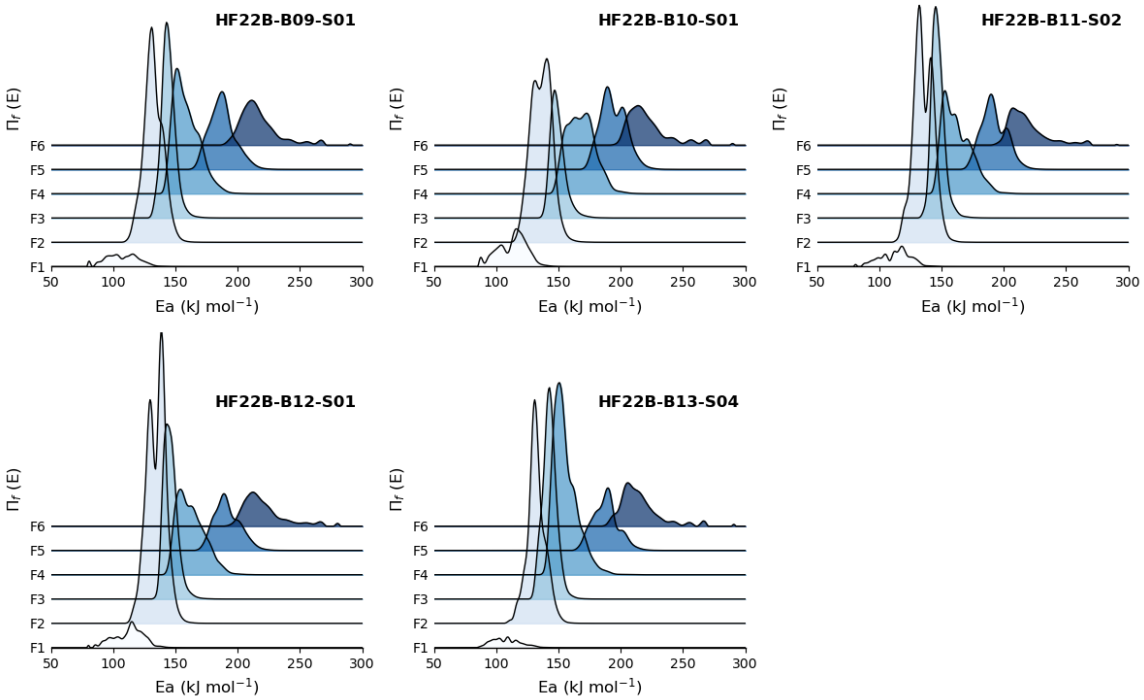

Figure S16. Characterization of sediment organic carbon (OC) activation energy obtained from Slow-RPO for the corresponding evolved gas fractions. Π_f (E) distributions for deposit OC in lateral accretion sets (f = 1, 2,. . ., 6). The sum of all Π_f (E) distributions in (b) yields the *p*(E) distribution of the corresponding bulk OC. Colour different gas fractions.

Estimating rates of organic carbon degradation in floodplain deposits

We considered the first-order degradation for *i*-OC by considering the initial *i*-OC concentration $C(0)_i$ and the concentration $C(t)_i$ at time t, the calculation can be explained by the following equation:

$$C(t)_i = C(0)_i e^{-kt} \quad (4)$$

where *e* is the natural number as the base, t is the duration of the reaction (yr), and *k* (yr^{-1}) is the rate constant of decomposition or decline of the corresponding materials. We did not set a real value for $C(0)$ but used a fitting by transforming equation (Methods), considering a constant density for all sediments $C(t)_i = \rho OC(t)_{Norm}$ and $C(0)_i = \rho OC(0)_{Norm}$, so $C(t)_i/C(0)_i = OC(t)_{Norm,i}/OC(0)_{Norm,i}$, and *i* represents the corresponding sediment or the bins by deposit age, then we can obtain:

$$OC(t)_{Norm}/OC(0)_{Norm} \cdot e^{-\int k(t)dt} \quad (5)$$

Through this approach, we then incorporate: (1) *k* is a constant, (2) the power law model: the effective time-dependent OC decay rate $k(t) = at^b$, which is equivalent to $\int k(t)dt = a/(b+1) \cdot t^{b+1}$. In the first case, we can obtain the model: $OC(t)_{Norm,i}/OC(0)_{Norm,i} = e^{-kt}$ to fit the OC degradation in LAS deposits over time (Fig. S17a). In the second case, the model is followed by Middelburg et al. (1989)[29] and Rothman and Forney (2007)[30], these studies demonstrated that the *k* for OC in marine sediments declines over time via distinct mechanisms. Here, we explored a similar logarithmic decline in *k* with time, integrated into a first-order kinetic model, motivated by our observations of increasing mean activation energy in buried OC with their radiocarbon

age. Then we can transform equation (5) to:

$$OC(t)_{Norm,i}/OC(0)_{Norm,i} = e^{\frac{-a}{b+1}t^{b+1}} \quad (6)$$

Both models provide good fits to the LIDET data, while no discernible trend is observed for the LAS data (Fig. S17). This pattern is consistent with the log-linear relationship described in the main text. Application of a first-order kinetic model of OC degradation, whether assuming a constant or time-dependent rate *k*, yields near-complete loss of the initial OC in the LIDET dataset over 6,000 years. However, in the LAS deposits, even assuming the model provides a valid prediction, OC loss is limited to ~3% under a constant *k* (three orders of magnitude lower compared to *k* of LIDET), and increases to ~32% when *k* is assumed to vary with time. These results show that OC storage in floodplain LAS deposits is highly efficient.

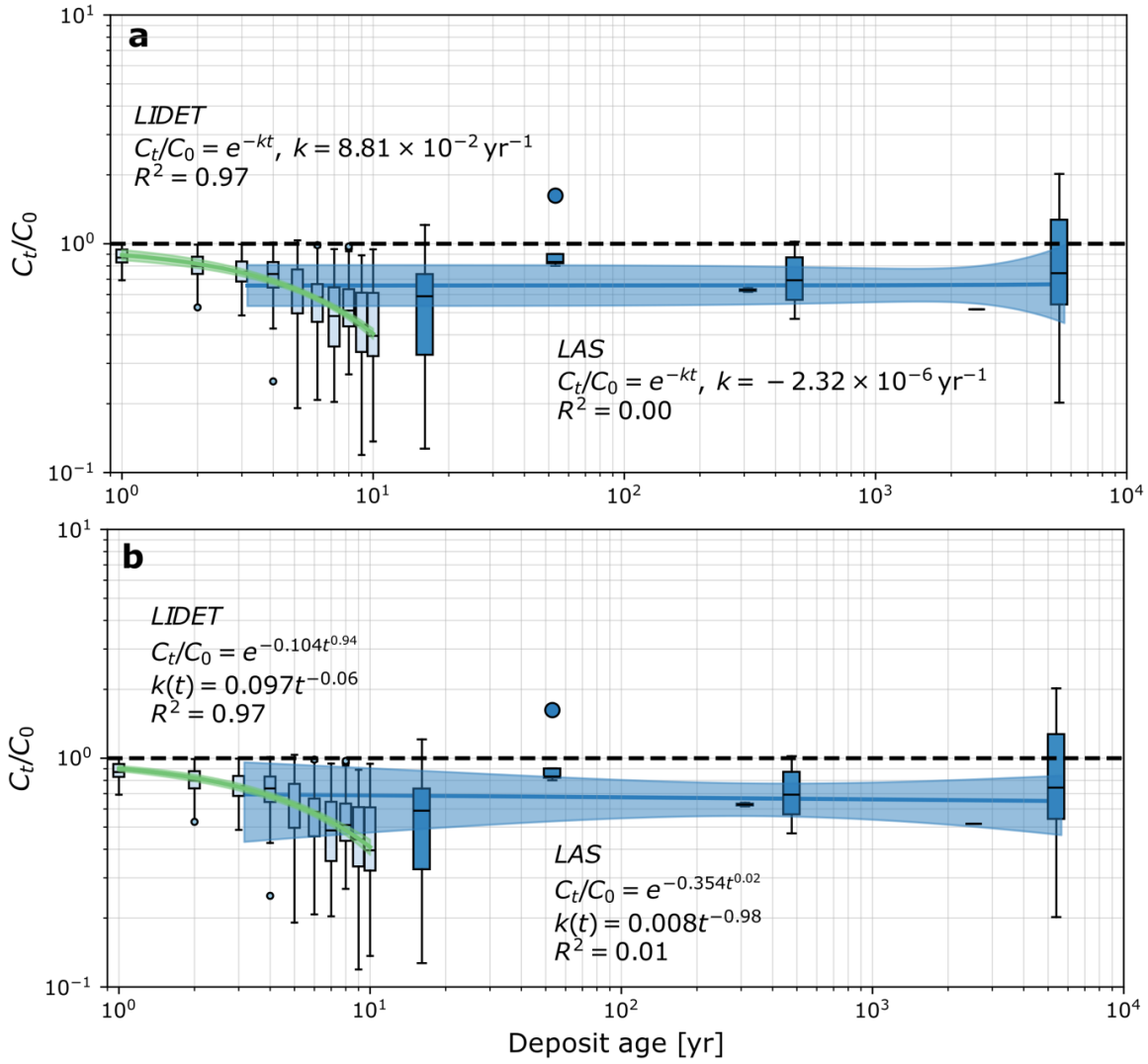

Figure S17. Degradation rates of OC in floodplains. (a) Assume the OC degradation parameter k is a constant. (b) Assume the OC degradation parameter k is a constant that is dependent on time. C_t/C_0 indicates the relative loss of OC through time t (deposit age). Bins in blue represent C_t/C_0 of LAS (see Methods); bin size is set to every half order of magnitude, and negligible degradation is observed across terrains spanning three orders of magnitude in age, from decadal to millennial timescales. Shown in green bins are the LIDET data from the Bonanza Creek site in Alaska, representing the decomposition kinetics of plant debris over 10 years in a similar Arctic terrestrial environment (LIDET, 1996[31], see Methods). The black dashed line represents C_t/C_0 equal to 1, as a reference line for OC decomposition extent. The boxplot consists of median values (central line and white circles), the interquartile range (IQR, represented by the box edges, which correspond to the 25th and 75th percentiles), and the whiskers, which extend to the most extreme data points within 1.5 times the IQR. To evaluate the relationship between OC degradation and deposit age, OC degradation was inferred using a first-order kinetic model. Regression in panel (a) follows the relationship $C_t/C_0 \propto e^{-kt}$, where k is a constant; regression in panel (b) follows the same relation, but with k changing with time: $k = at^b$. Regression lines and their 90% confidence intervals were backtransformed and plotted in blue (LAS) and green (LIDET), respectively.

Supplementary References

1. Sylvester, Z., Durkin, P. & Covault, J. A. High curvatures drive river meandering. *Geology* **47**, 263–266 (2019).
2. Rowland, J. C. *et al.* A morphology independent methodology for quantifying planview river change and characteristics from remotely sensed imagery. *Remote Sens. Environ.* **184**, 212–228 (2016).
3. Lee, T. C., Kashyap, R. L. & Chu, C. N. Building Skeleton Models via 3-D Medial Surface Axis Thinning Algorithms. *CVGIP Graph. Models Image Process.* **56**, 462–478 (1994).
4. Sakoe, H. & Chiba, S. Dynamic programming algorithm optimization for spoken word recognition. *IEEE Trans. Acoust. Speech Signal Process.* **26**, 43–49 (1978).
5. Ielpi, A. *et al.* How Is Time Distributed in a River Meander Belt? *Geophys. Res. Lett.* **50**, e2022GL101285 (2023).
6. Geyman, E. C., Douglas, M. M., Avouac, J.-P. & Lamb, M. P. Permafrost slows Arctic riverbank erosion. *Nature* **634**, 359–365 (2024).
7. Geyman, E. *et al.* Quantifying river migration rates in the Yukon River Watershed from optical satellite imagery, Alaska, 2016-2022. (2024).
8. Geyman, E. C. *et al.* Scaling laws for sediment storage and turnover in river floodplains. *Sci. Adv.* **11**, eadu8574 (2025).
9. Douglas, M. *et al.* Geomorphic mapping and permafrost occurrence on the Koyukuk River floodplain near Huslia, Alaska. (2023).
10. Callahan, B. J. *et al.* DADA2: High-resolution sample inference from Illumina amplicon data. *Nat. Methods* **13**, 581–583 (2016).
11. Callahan, B. DADA2 pipeline tutorial (1.16). (2023).
12. Bush, R. T. & McInerney, F. A. Leaf wax *n*-alkane distributions in and across modern plants: Implications for paleoecology and chemotaxonomy. *Geochim. Cosmochim. Acta* **117**, 161–179 (2013).
13. Dion-Kirschner, H., McFarlin, J. M., Masterson, A. L., Axford, Y. & Osburn, M. R. Modern constraints on the sources and climate signals recorded by sedimentary plant waxes in west Greenland. *Geochim. Cosmochim. Acta* **286**, 336–354 (2020).
14. Hollister, K. V. *et al.* Aquatic and Terrestrial Plant Contributions to Sedimentary Plant Waxes in a Modern Arctic Lake Setting. *J. Geophys. Res. Biogeosciences* **127**, e2022JG006903 (2022).
15. Diefendorf, A. F., Freeman, K. H. & Wing, S. L. Distribution and carbon isotope patterns of diterpenoids and triterpenoids in modern temperate C3 trees and their geochemical significance. *Geochim. Cosmochim. Acta* **85**, 342–356 (2012).
16. Mao, D. *et al.* Resolving the unresolved complex mixture in motor oils using high-performance liquid chromatography followed by comprehensive two-dimensional gas chromatography. *Fuel* **88**, 312–318 (2009).

17. Hemingway, J. D. *et al.* Mineral protection regulates long-term global preservation of natural organic carbon. *Nature* **570**, 228–231 (2019).
18. Cui, X. *et al.* Global fjords as transitory reservoirs of labile organic carbon modulated by organo-mineral interactions. *Sci. Adv.* **8**, eadd0610 (2022).
19. Hemingway, J. D. *et al.* Assessing the Blank Carbon Contribution, Isotope Mass Balance, and Kinetic Isotope Fractionation of the Ramped Pyrolysis/Oxidation Instrument at NOSAMS. *Radiocarbon* **59**, 179–193 (2017).
20. LaRowe, D. E. & Van Cappellen, P. Degradation of natural organic matter: A thermodynamic analysis. *Geochim. Cosmochim. Acta* **75**, 2030–2042 (2011).
21. Blair, N. E. & Aller, R. C. The Fate of Terrestrial Organic Carbon in the Marine Environment. *Annu. Rev. Mar. Sci.* **4**, 401–423 (2012).
22. Ruben, M. *et al.* Fossil organic carbon utilization in marine Arctic fjord sediments by subsurface micro-organisms. *Nat. Geosci.* 1–6 (2023) doi:10.1038/s41561-023-01198-z.
23. Soulet, G. *et al.* Temperature control on CO2 emissions from the weathering of sedimentary rocks. *Nat. Geosci.* **14**, 665–671 (2021).
24. Hemingway, J. D. *et al.* Microbial oxidation of lithospheric organic carbon in rapidly eroding tropical mountain soils. *Science* **360**, 209–212 (2018).
25. Petsch, S. T., Eglinton, T. I. & Edwards, K. J. 14C-Dead Living Biomass: Evidence for Microbial Assimilation of Ancient Organic Carbon During Shale Weathering. *Science* **292**, 1127–1131 (2001).
26. Strauss, J. *et al.* Organic-matter quality of deep permafrost carbon – a study from Arctic Siberia. *Biogeosciences* **12**, 2227–2245 (2015).
27. Galy, V., Peucker-Ehrenbrink, B. & Eglinton, T. Global carbon export from the terrestrial biosphere controlled by erosion. *Nature* **521**, 204–7 (2015).
28. Blair, N. *et al.* Carbon isotopic fractionation in heterotrophic microbial metabolism. *Appl. Environ. Microbiol.* **50**, 996–1001 (1985).
29. Middelburg, J. J. A simple rate model for organic matter decomposition in marine sediments. *Geochim. Cosmochim. Acta* **53**, 1577–1581 (1989).
30. Rothman, D. H. & Forney, D. C. Physical Model for the Decay and Preservation of Marine Organic Carbon. *Science* **316**, 1325–1328 (2007).
31. Harmon, M. E. LTER Intersite Fine Litter Decomposition Experiment (LIDET), 1990 to 2002 ver 11. Environmental Data Initiative https://doi.org/10.6073/pasta/f35f56bea52d78b6a1ecf1952b4889c5 (2016).